Title

A 3-D Active Contour Method for Automated Segmentation of the Left Ventricle From Magnetic Resonance Images.

Permalink

https://escholarship.org/uc/item/2f4469m4

Journal

IEEE transactions on bio-medical engineering, 64(1)

ISSN

0018-9294

Authors

Hajiaghayi, Mahdi
Groves, Elliott M
Jafarkhani, Hamid
et al.

Publication Date

2017

DOI

10.1109/tbme.2016.2542243

Peer reviewed

A 3D Active Contour Method for Automated Segmentation of the Left Ventricle from Magnetic Resonance Images

Mahdi Hajiaghayi, *Ph.D.*, Elliott M. Groves, *M.D., M.Eng.*, Hamid Jafarkhani, *Ph.D.*, *Fellow, IEEE* and

Arash Kheradvar, *M.D. Ph.D.*

Abstract— Objective: **This study's objective is to develop and validate a fast, automated 3D segmentation method for cardiac Magnetic Resonance Imaging (MRI). The segmentation algorithm automatically reconstructs cardiac MRI DICOM data into a 3D model (i.e., direct volumetric segmentation), without relying on prior statistical knowledge.** *Methods:* **A novel 3D active contour method was employed to detect the left ventricular cavity in 33 subjects with heterogeneous heart diseases from the York University database. Papillary muscles were identified and added to the chamber using a convex hull of the left ventricle and interpolation. The myocardium was then segmented using a similar 3D segmentation method according to anatomic information. A multi-stage approach was taken to determine the method's efficacy.** *Results:* **Our method demonstrated a significant improvement in segmentation performance when compared to manual segmentation and other automated methods.** *Conclusion and Significance*: **A true 3D reconstruction technique without the need for training datasets or any user-driven segmentation has been developed. In this method, a novel combination of internal and external energy terms for active contour was utilized that exploits histogram matching for improving the segmentation performance. This method takes advantage of full volumetric imaging, does not rely on prior statistical knowledge and employs a convex hull interpolation to include the papillary muscles.**

Index Terms— **Cardiac MRI, Segmentation, Automated, Three dimensional, Volumetric, Active contour method**

I. INTRODUCTION

CARDIAC Magnetic Resonance (CMR) imaging is a robust modality that does not employ ionizing radiation or iodinated contrast but delivers images with high spatial resolution. Currently, many of the commercially available software platforms for CMR post-processing either provide suboptimal automated segmentation or require a substantial amount of manual segmentation effort from the operator, resulting in significant methodological variability [1-3]. Even the most recently released commercial CMR analysis tools only report themselves to be semi-automated, which can lead to a great deal of inter-observer variability and thus diminish CMR's clinical utility [4]. Moreover, manual segmentation is time consuming and requires dedicated operator training that makes it inefficient due to the extent of information in CMR images [5, 6]. Nevertheless, the current gold standard for assessment of ventricular function based on MRI is manual segmentation by a trained physician, as automated techniques currently lack the necessary accuracy.

Most cardiac segmentation techniques treat 2D segmentation and 3D multiplanar reconstruction as two separate processes [7-9]. These processes achieve volumetric reconstruction by first applying a 2D segmentation approach independently for each slice, and then volumizing these 2D segmented image stacks into 3D objects. This procedure only considers volumizing a particular set of images (e.g., short axis or sagittal stack). Therefore, the procedure loses some important details of the object, generally resulting in objects with significant inaccuracies [10, 11]. Here, volumizing refers to 3D reconstruction of the volume of a chamber from segmented images.

In this study, we have developed a true 3D reconstruction technique without the need for training datasets or any user-driven segmentation. This method exploits the benefit of full volumetric imaging, and does not rely on prior statistical knowledge.

II. METHODS

The input to the algorithm is a stack of either short- or long-

axis CMR images, or any standard sagittal, coronal, and axial MR images, and the output is a refined point cloud representing the cardiac chamber being segmented.

A. CMR Data

Our algorithm can utilize either short or long-axis CMR images or images from a standard MRI in any plane (axial, coronal, sagittal) as long as they encompass the heart. The initial CMR data to develop and test our algorithm was acquired using an axial gradient-echo fast low-angle shot sequence with readout of 512 and a gap of 0.8 mm between slices from normal subjects on a Phillips Medical System Achieva 3T scanner. The manual segmentation of these CMR images was performed by a board certified cardiologist with formal CMR segmentation training. The left ventricle (LV) was segmented at both end-diastole and end-systole.

The second set of data used for comparison was a CMR dataset from Department of Diagnostic Imaging of the Hospital for Sick Children in Toronto, Canada available from the York University website[*] [12]; here referred to as York database. This database contains short axis cardiac MR images from 33 subjects together with their manual segmentations of endocardial and epicardial contours performed by an experienced cardiologist. The York database consists of a heterogeneous group of subjects with normal hearts and congenital heart diseases with a mean age of 12.0±4.0 (Table 1).[†]

For quantitative validation of our 3D segmentation method, a phantom of a human LV was constructed with a known volume. The phantom was imaged on a Phillips Medical System Achieva 3T scanner with a breast coil. The image dimensions were 512 × 512 and 2D images were acquired at slice thicknesses and x and y spacing, respectively, of 1 mm, 0.234mm and 0.235mm.

B. Reconstruction Methodology

Our method is carried out over three consecutive steps, as summarized in Figure 1:

The first step is endocardial segmentation where the algorithm generates a 3D estimation of a heart chamber (e.g., LV) using an adaptation of the active contour method [13, 14]. To start this process, an arbitrary point in the chamber on a 2D slice from the CMR image stack is randomly selected. Centered at that point, a contour ball that grows is initiated until it converges to the internal borders of the chamber.

The second step is intra-chamber inclusion using convex hull interpolation where the algorithm modifies the result by adding intra-chamber structures (e.g., LV's papillary muscles) that most automated segmentation algorithms exclude from the chamber [11, 15-17].
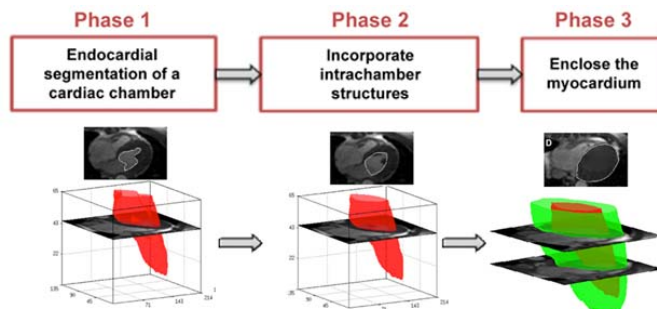

Fig. 1. Three steps (phases) of the segmentation method: Step 1 segments the endocardial layer of a cardiac chamber; Step 2 incorporates intra-chamber structures; Step 3 defines the myocardium.

During the third step, myocardial segmentation is performed and the algorithm identifies the enclosing myocardium using the 3D segmentation introduced in the first step with some modifications to be further discussed. Figure 1 illustrates these three steps:

Step I: Endocardial Segmentation of a Cardiac chamber using 3D Active Contour Segmentation

3D active contours are dynamic surfaces that evolve and move toward an object of interest and eventually lie on its edges. To mathematically represent such a surface in a 3D domain, we employ a signed distance function (SDF) $\Phi(v)$ for all voxels $v = (x, y, z)$ in the image domain Ω [18]. For a closed contour, this function returns negative values for the voxels inside the contour and positive values for the voxels outside. Evolution of the active contour is driven by minimizing an energy function $E(\Phi)$ designed to reach its minimum when the contour lies on the boundary of the object of interest. The $E(\Phi)$ generally includes two components:

TABLE I
SUBJECTS DEMOGRAPHIC INFORMATION

Subject#	Age (year)	Diagnosis
1	16	Right Ventricular Outflow tract (RVOT) enlargement
2	14	Arrhythmogenic Right Ventricular Dysplasia (ARVD)
3	14	Tetralogy of Fallot (TOF) / RVOT enlargement
4	12	Unknown
5	13	Coarctation of Aorta
6	9	Coarctation of Aorta
7	16	Marfan Disease
8	15	Coarctation of Abdominal Aorta
9	14	Right Ventricular Volume Overload
10	14	Atrial Septal Defect
11	Unknown	Unknown
12	2	ARVD
13	11	ARVD
14	9	ARVD
15	6	Familial History of sudden death; ARVD
16	8	ARVD
17	12	TOF with dilated pulmonary artery stenosis
18	17	Normal
19	2	Coronary Artery Aneurysm
20	11	Peripheral Artery Stenosis
21	8	Cardiomyopathy
22	17	Left Ventricular Hypertrophy (LVH); Coarctation of Aorta
23	16	Myocardial Infarction (MI)
24	16	Bileaflet Aortic Valve; moderate Aortic Regurgitation
25	13	Normal
26	9	Severe Aortic Insufficiency
27	16	LVH
28	12	Right Ventricular MI
29	13	Dextro-Transposition of the Great Arteries
30	13	Truncus Arteriosus
31	16	RVOT Tachycardia
32	15	ARVD
33	7	Ventricular Tachycardia (potential ARVD)

[*] http://www.cse.yorku.ca/~mridataset/

[†] http://www.cse.yorku.ca/~mridataset/metadata.txt

$$E(\Phi) = E_{int}(\Phi) + E_{ext}(\Phi), \quad (1)$$

where E_{int} and E_{ext} are the internal and external energy functions, respectively. E_{int}, whose minimization shrinks the contour's surface, plays a regulating role to control the contour's smoothness. The internal energy function for a SDF Φ is described as:

$$E_{int}(\Phi) = w_1 \sum_{v \in \Omega} |\nabla H(\Phi(v))|, \quad (2)$$

where ∇ and $|.|$ denote gradient and absolute value operators, respectively; $H(x): \mathbb{R} \to \mathbb{R}$ is the Heaviside step function with $H(x) = 1$ for $x > 0$ and $H(x) = 0$ otherwise [17], [19]. Accordingly, $H(\Phi(v))$ is 0 inside and 1 outside of the contour, and thus $|\nabla H(\Phi(v))| = 1$ at the border and 0 elsewhere. From here on, we drop v from $\Phi(v)$ for the sake of brevity. E_{ext} is a data-driven term that provides information about the object boundaries and plays a driver role. For example, for LV segmentation, we use the following external energy function:

$$E_{ext}(\Phi) = w_2 E_{reg} + w_3 E_{edge} + w_4 E_{geom}, \quad (3)$$

which is a combination of the region-based (E_{reg}), edge-based (E_{edge}) and geometric terms (E_{geom}) to be introduced shortly. The weights, w_i's $i = 1, \cdots, 4$, are carefully chosen for each image and should add up to 1. While the effect of weighting parameters can be negligible for some object segmentations, these parameters are more sensitive in CMR segmentation. No quantitative analysis or straightforward strategy currently exists to yield the optimal weighting parameters for segmentation. In our method, we often pursue a trial and error approach to obtain these parameters. However, once the optimal weighting parameters are found for one cardiac MR image, they can be used for the whole image stack without compromising the performance. The region-based term (E_{reg}) from Equation (3) calculates how likely a voxel v belongs to the foreground (myocardium) or background (blood pool) given its signal density [17]. This term in a general form is represented by:

$$E_{reg} = -\sum_{v \in \Omega} (\log p(I(v)|\Omega_F)(1 - H(\Phi)) + \log p(I(v)|\Omega_B)H(\Phi)) \quad (4)$$

where $I(v)$ denotes the signal intensity at voxel v., $p(.|\Omega_F)$ and $p(.|\Omega_B)$ are myocardium and blood pool probability density functions (PDFs), respectively. If they are not known a priori, they are replaced by the PDFs of inside and outside of the active contour, usually modeled by Gaussian distributions with different means and variances. As the contour evolves, the means and variances are both updated. In Appendix A, E_{reg} along with the Gaussian PDF and the details of the updating process are further described.

The edge-based term (E_{edge}) detects the objects' edges [20]:

$$E_{edge} = \sum_{v \in \Omega} g(I(v))|\nabla H(\Phi)|, \quad (5)$$

where $g(I)$ can be any function whose minimum occurs at the edge of the object of interest [18]. Here we consider $g(I) = (1 + \beta \nabla(G_\sigma * I))^{-1}$, where $G_\sigma * I$ is the convolution of the image I and a 3-D Gaussian kernel with parameter σ. In this case, $g(I)$ has an inverse relationship with ∇I, thus reaching a much lower value on the edges compared to the homogeneous regions. The parameters β and σ can be set using trial and error. We reached the values $(\beta, \sigma) = (100, 15)$ and used them throughout our numerical experiments. We observed that these values work well for all CMR images in our database.

The geometric term (E_{geom}) sets geometrical constraints on the active contour. A common problem related to the non-model-based segmentation approaches is the leakage around the weak or missing boundaries. This is particularly observed in CMR image segmentation. One way to avoid this leakage is to set a geometrical constraint on the active contour. For example, it is known that LV is roughly axisymmetric considering the heart's short-axis, and this constrain can be used in segmentation. The same argument is used for the whole 3D segmentation. We use this through a symmetric constraint on the LV's short-axis defined as:

$$E_{geom} = \underbrace{\left| \frac{\sum_{v \in \Omega}(x - x_0)(1 - H(\Phi))}{\sum_{v \in \Omega}(1 - H(\Phi))} \right|}_{E_{geom}^{(x)}} + \underbrace{\left| \frac{\sum_{v \in \Omega}(y - y_0)(1 - H(\Phi))}{\sum_{v \in \Omega}(1 - H(\Phi))} \right|}_{E_{geom}^{(y)}} \quad (6)$$

A similar term has also been introduced by Wang *et al.* [21]. This function calculates the x and y spatial deviation of the geometrical center of the active contour C from the centroid point's x_0 and y_0, to be further described. The active contour problem seeks a unique contour denoted by C^*, which lies on the boundary of the object of interest. This problem translates into the underlying minimization problem over Φ:

$$\Phi^* = \arg\min_{\Phi}(E_{int}(\Phi) + E_{ext}(\Phi)) \quad (7)$$

for which we employ the gradient descent algorithm to solve. The gradient descent first starts with a 3D initialization matrix $\Phi^0(v)$, for $v \in \Omega$, followed by updating Φ via

$$\Phi^{k+1} = \Phi^k - \Delta t^k \left(\frac{\partial E_{int}}{\partial \Phi} \Big|_{\Phi^k} + \frac{\partial E_{ext}}{\partial \Phi} \Big|_{\Phi^k} \right), \quad (8)$$

where Δt, the step size, is chosen wisely to ensure convergence and stability. Both E_{ext} and E_{int} are functionals (function of functions), and their derivatives, which are required for the gradient descent algorithm are calculated using the Euler-Lagrange equality. This equality states that if $F(\Phi) = \sum_v f(v, \Phi, \Phi_v(v))$ for any integer function f, the derivative of F with respect to Φ is calculated as:

$$\frac{\partial F}{\partial \Phi} = \frac{\partial f}{\partial \Phi} - \frac{\partial}{\partial v} \frac{\partial f}{\partial \Phi_v}. \quad (9)$$

In Appendix B, the derivative of E_{int} and all terms of E_{ext}, which include E_{reg}, E_{edge} and E_{geom} are further described.

These derivatives are computed for each voxel $v \in \Omega$, and expressed as 3D matrices. To construct the initial distance function Φ^0, a random point inside the LV is selected and a contour ball is considered whose respective signed distance function forms Φ^0. The x and y dimensions of this point can also be used as (x_0, y_0) for the geometric term.

Each iteration of the gradient descent algorithm updates the function Φ for each voxel. However, this update may not maintain the sign distance property of Φ; accordingly, we must frequently reinitialize [22]. This process is fully automatic and no user interaction is required. The final Φ^* yields the final contour C^*. As it is not mathematically simple to represent a 3D contour, we use the SDF function, Φ, which has a one-to-one mapping with C. This mapping is as follows: Given Φ, all the points that have zero value specify the contour. That is,

$$C = v \in R^3, \Phi(v) = 0 \quad (10)$$

Once Φ^* is known, the mapping is used to obtain C^*. Figure 2 depicts the evolution of the LV's 3D contour during the first phase of the algorithm.
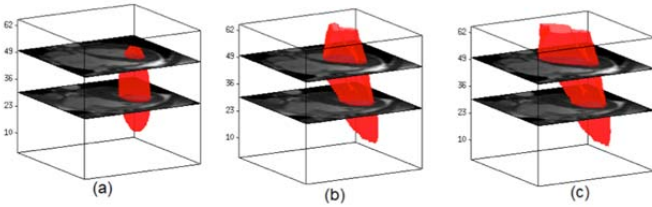

Fig. 2. Illustration of the left ventricular contour evolution: (A) in early iteration; (B) mid iteration; and (C) final iteration of the gradient descent algorithm.

To ensure the convergence and numerical stability of an upwind scheme, Δt must satisfy the Courant, Friedrichs, Lewy (CFL) condition [23]. This condition requires Φ to change no further than a pixel space after each time step, thus choosing Δ_t^k as:

$$\Delta_t^k = 0.45 \left(max_{v \in \Omega} \frac{\partial F}{\partial \Phi} |_{\Phi^k} \right)^{-1} \quad (11)$$

This would satisfy the CFL condition. The weighting parameters $w_1, \dots, w_4$ play a paramount role in achieving a desirable segmentation result. For example, a high w_1 favors the internal energy term that excessively smoothes the shape that creates inherent inaccuracies. The optimal weights for an image are conventionally obtained through a trial and error procedure. Once the optimal weighting parameters are found for one CMR image, they can be used for the whole stack without any degradation in quality. The optimal weighting parameters obtained for the reference image can be used for a new image as long as the two images are normalized. We use histogram matching for this purpose [24]. For a new image, first its signal intensity histogram is matched to the reference image, and then uses the weights of the reference image for the new image. Histogram matching with fixed weights significantly improves the performance of the segmentation algorithm.

Step II: Intra-chamber Inclusion using Convex Hull Interpolation

Due to the homogeneous signal intensity of intra-chamber structures (e.g., LV's papillary muscles) and the surrounding myocardial structure, many segmentation techniques exclude these structures from the chamber [15-17, 25]. Our method identifies these structures and adds them back to the reconstructed volume.

For each 2D slice, the algorithm considers the contour obtained from the previous phase. Due to the exclusion of the intra-chamber structures, this contour is non-convex, meaning that the line connecting any two points inside the contour is not necessarily inside the contour. We argue that the points on the convex border can be interpolated to refine the segmentation (Figure 3). To do so, the points on the contour's convex hull are first identified [26]. Given N points $(x_1, y_1), \dots, (x_N, y_N)$, the centroid is obtained as

$$c = (\frac{1}{N} \sum_{i=1}^{N} x_i, \frac{1}{N} \sum_{i=1}^{N} y_i) \quad (12)$$

This centroid point is used as the center of the cylindrical coordinates, and the radius and angle of all points on the convex hull are calculated according to the new coordinate system. Let $r_1, r_2, \dots, r_N$ and $\theta_1, \theta_2, \dots, \theta_N$ denote the radii and angles of these points, respectively, with r_i and θ_i representing the distance and angle of the ith point with regard to the center (θ_is unequally spaced).
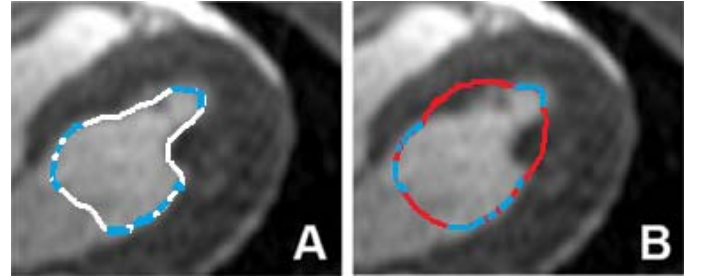

Fig. 3. (A) shows a 2D cross-section of the first phase segmentation while (B) shows the convex hull of the segmentation, which includes the papillary muscles (red curves). The blue dots on the LV border specify the convex hull. The red curve illustrates the output of the linear interpolation of the blue points in the cylindrical coordinates. The initial point is chosen at a random MR slice, and its location does not affect the final segmentation results.

Once the cylindrical coordinates of the convex hull points are determined, the r versus θ scatter plot would be considered, and fit to a parabolic curve using piece-wise interpolation such that for equally-spaced $\theta'_1, \theta'_2, \dots, \theta'_M$, their corresponding $r'_1, r'_2, \dots, r'_M$ is obtained. This new set of points constructs a closed convex curve that best approximates the non-convex chamber contour and includes the intra-chamber structures (Figures 3 and 4). This modification over the LV volume is shown in Figure 4B, providing a more accurate representation of the LV geometry.
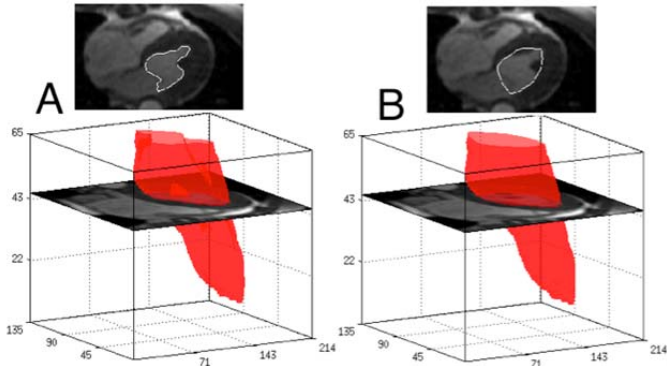
Fig. 4. (A) The 3D segmentation of the left ventricle prior to Phase 2, vs. (B) after Phase 2 (convex hull interpolation). This figure shows how the papillary muscles are incorporated using the convex hull interpolation. Two cross-sections with and without papillary muscles are provided for better clarification. The background images on top are long axis view.

Step III: Myocardial Segmentation

This step extracts the myocardium as the foreground from the rest of the CMR image. We follow the 3D segmentation method discussed in Step I with slight changes in the external energy function. Once the enclosing chamber is segmented, as in Step I, and its boundaries are detected, the algorithm removes the endocardium and refills it with the grey-scale intensity of the myocardium that surrounds the chamber as shown in Figure 5.
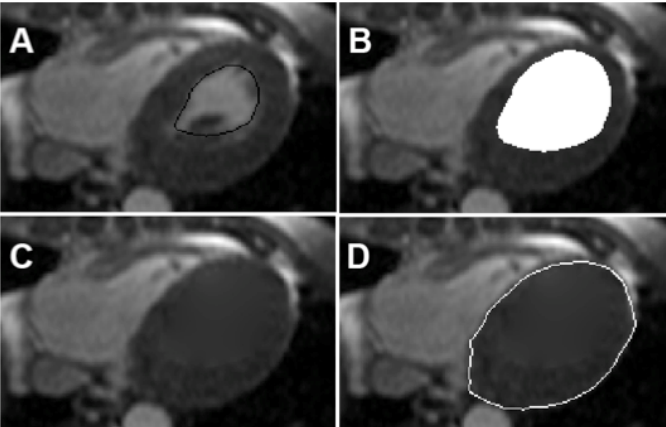

Fig. 5. A cross-section of 3D segmentation procedure during Step III: (A) is a result of Step II; (B) removing the intra-chamber area; (C) refilling with the myocardium; (D) white line shows enclosing left ventricle with all of its contents (two-chamber view).

The hull of Figure 5B shows the area to be refilled with the gray-scale intensity. To do so, the algorithm moves a few pixels away from the endocardial boundary and then performs the refilling procedure. This expansion from the endocardial boundary in Figure 5A to 5B ensures that the algorithm does not overlook any endocardial pixels. Additionally, it allows the segmentation to reach to the region of the myocardium and use its grey-scale intensity for refilling. To do so, we interpolate inward using the grey-scale intensities densities by solving Laplace's equation. This refilling procedure produces a homogeneous region of segmented myocardium that includes the endocardium.

Next, the algorithm applies the 3D segmentation method previously discussed in Step I to find the endocardial borders.

However, unlike Step I, we now have a rough estimate of the density histogram distribution of the foreground (myocardium) and background (the rest of the chamber). Sample voxels are automatically selected from the myocardial area without any operator interaction. To find the background sample points, the focus would be on the points far from the centroid. The algorithm moves along the radial lines of the equally-spaced angles to obtain both foreground and background sample points.
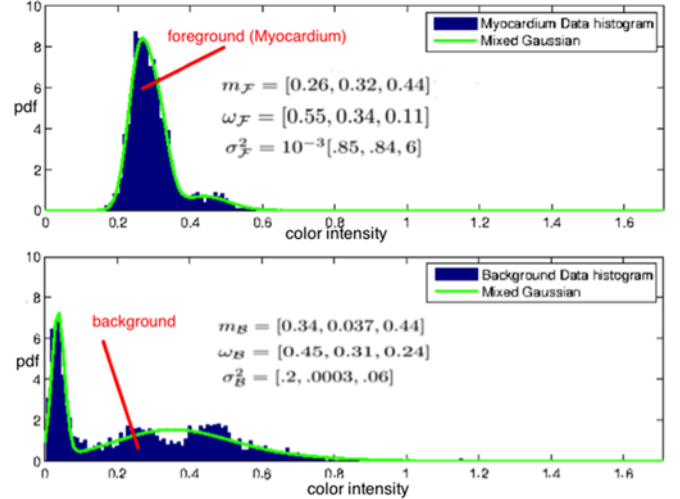

Fig. 6. PDF estimation of histogram sample of myocardium and the background using the expected maximization (EM) method.

Once these sample voxels are known, the foreground and background PDFs ($p(.|\Omega_F)$ and $p(.|\Omega_B)$) are found in a region-based term as shown in Figure 6. We consider a Gaussian mixture model with $K = 3$ Gaussian components $N(x; m_{is}, \sigma^2)$ to represent $p(.|\Omega_F)$ and $p(.|\Omega_B)$, i.e.,

$$p(I(v)|\Omega_s) = \sum_{i=1}^{K} \frac{\omega_{is}}{\sigma_{is}\sqrt{2\pi}} e^{\frac{(I(v)-m_{is})^2}{\sigma_{is}^2}}, \qquad s \in F, B \quad (13)$$

with parameters $\omega_{is}, m_{is}, \sigma_{is}^2$ representing the weight, the mean, and the variance of the ith component of the foreground ($s = F$) and the background ($s = B$). These parameters can be
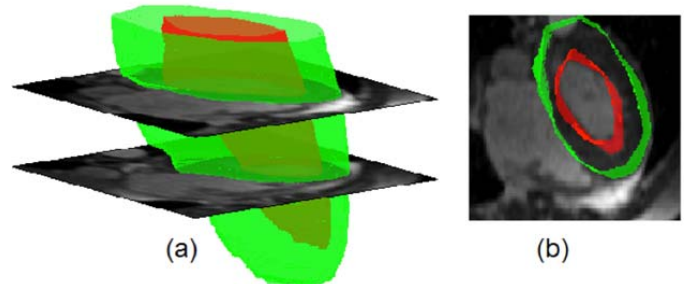

Fig. 7. Volumetric segmentation of the left ventricle; (a) perspective view; (b) top view.

identified using the expected maximization (EM) method from the sample voxels obtained earlier [27]. Note that one may increase the number of Gaussian components with the hope of better performance; however, this increase may not always lead to a better performance. Additionally, the higher the number of components, the longer it takes to calculate the distribution parameters. We

reached to $K = 3$ based on the quality of our image database, and the time complexity of the outcome. Figure 6 depicts a histogram sample of the myocardium and the background. It also shows how the estimated Gaussian mixture model with obtained parameters fits this histogram. Once the PDF parameters are determined, they remain fixed over all iterations and unlike Step I, there is no need to update them (Figure 7).

III. RESULTS

To validate our algorithm, a multi-stage approach was taken that involved a direct comparison to manually segmented images, a phantom experiment, and a comparison to two other automated techniques. Finally, we tested the effects of contrast to noise ratio (CNR) and signal to noise ratio (SNR) on the algorithm.

A. Validation with Manual Segmentation

For validation purposes, we compared LV volumes obtained from manual segmentation (V_{man}) with the data obtained from our automatic technique V_{auto}. The short axis sequences were utilized in segmentation of the studied subjects. Simpson's rule was employed to compute the volume. This method needs to include the pixel-spacing and slice-spacing of the 3D image extracted from the CMR data. We also used the Dice metric given by $2 \times \frac{V_{man} \cap V_{auto}}{V_{man} + V_{auto}}$. This metric is in fact the F1 metric in the context of machine learning.

B. Validation with York Database

CMR dataset from Department of Diagnostic Imaging of the Hospital for Sick Children in Toronto, Canada was used for validation. We achieved between 80% to 90% accuracy in estimating LV volumes in 13 out of 33 subjects compared to the ground truth. Only in 6 cases, our estimate fell below 70% accuracy.

There was one outlier, and if we excluded that, the mean accuracy of the dataset would be 76% ± 8%. Overall, in 27 out of 33 subjects, our algorithm provided a segmentation accuracy

higher than 70% with an average of 80% ± 5%. Figure 8 shows the reliability function –i.e., the complementary cumulative distribution function (ccdf)– of the obtained F1 accuracy [28]. As can be inferred from the figure, the convex hull interpolation significantly improves the performance. The convex hull interpolation improved the accuracy by almost 10% (i.e., 76% ± 8% with convex hull vs. 67% ± 13% without). A paired t-test showed that this improvement was statistically significant with a p-value less than 0.0001.

C. Comparison to Manual Segmentation and Alternate Reconstruction Algorithms

To further test our algorithm's functioning objectively, we compared its performance with that of two popular automatic cardiac segmentation methods using the York database. The first method was developed by Grosgeorge *et al.* [14] and the second method was developed by Mille *et al.* [29] and Pluempitiwiriyawej *et al.* [17]. Both methods were implemented by following the algorithms from their published work. However, some small discrepancies may still exist due to different initialization and other parameters involved.

Our method provides a 3D active contour model that fits into the cardiac MRI context more accurately. Grosgeorge's method neglects both edge and geometric terms. Additionally, the same variance was assumed for the foreground (LV) and background (rest of the CMR image) probability density functions. Our method considers the foreground and background pertaining to two different texture regions, thus adopting different variances, which is far more accurate. The methods developed by Mille *et al.* and Pluempitiwiriyawej *et al.* are quite identical as both consider an edge-based term and a region-based term but not a proper geometric term. In contrast to our method, neither method employs histogram matching or convex-hull interpolation. Both histogram matching and convex-hull contribute significantly to the performance improvement.
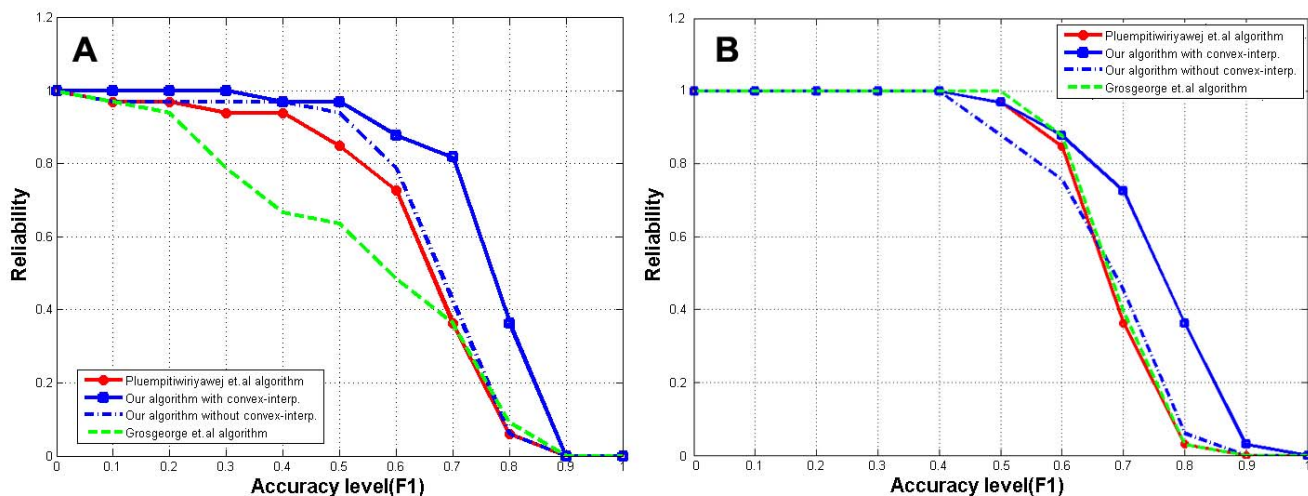

Fig. 8. A graphical representation of the reliability analysis for our method with and without convex hull interpolation, as well as the methods developed by Mille *et al.* [29] and Pluempitiwiriyawej *et al.* [17], and Grosgeorge *et al.* [14]. (A) at end-diastole; (B) at end-systole.

Figure 9 illustrates that a 3D model of the LV obtained from our method looks much more like a natural LV cavity than the manual segmentation as the manual segmentation is inherently inaccurate, and several studies have shown that it can be imprecise with a low level of reproducibility [30, 31].
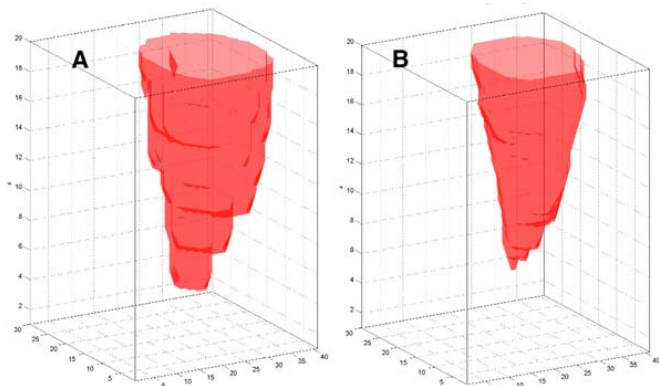

Fig. 9. Manual segmentation by a trained operator (A) vs. our method's output (B) for Patient 11 of York dataset.

Figure 8 provides a reliability analysis of F1 accuracy for all the methods including our algorithm using the subjects of the York database at end-diastole and end-systole. The method developed by Grosgeorge *et al.* resulted in an accuracy of 55% ± 23% and the method developed by Mille *et al.* and Pluempitiwirijawej *et al.* had an accuracy of 63% ± 16%, respectively. Our algorithm shows a statistically significant improvement in accuracy (both p-values <0.0001) and outperforms the other two methods [14, 17, 29].

D. Effects of Change in CNR and SNR

TABLE II
THE PARAMETERS VALUE FINE-TUNED FOR THE REFERENCE IMAGE.

Parameter	Value [a]
w_1	0.0093
w_2	0.045
w_3	0.0093
w_4	0.93
β	100
σ	15

Studying the effects of change in CNR and SNR was accomplished by introducing additive noise to a set of MRI datasets (in this example, we chose Patients 4, 5, 13, 14, 15, 19, 29 of the York database). Here, we tested how the algorithm's performance is affected as CNR and SNR decrease. This set of patients was chosen due to their higher image quality, which allowed considerable noise to be added before the data became uninterpretable. For a CMR dataset of poor quality, the initial segmentation result is not robust enough to support adding a significant level of noise.

Figure 10 shows the performance of our algorithm as a function of additive Gaussian noise. Predictably, performance drops as

the level of noise increases, or inversely, when the SNR or CNR decreases. However, the algorithm continues to perform well despite the addition of noise to certain level. It is not generally straightforward to report an operating CNR or SNR for these types of studies since there are other parameters involved in the performance that directly correlate with the CNR (e.g., SNR, the weighting parameters, or initialization of the algorithm that makes it hard to give a number for operating CNR). Finally, introduction of significant noise (i.e., greater than -10 dB) led to a considerable decline in the algorithm's performance; however, that level of noise would likely render a study uninterpretable regardless of the method of segmentation (i.e., manual or automatic).
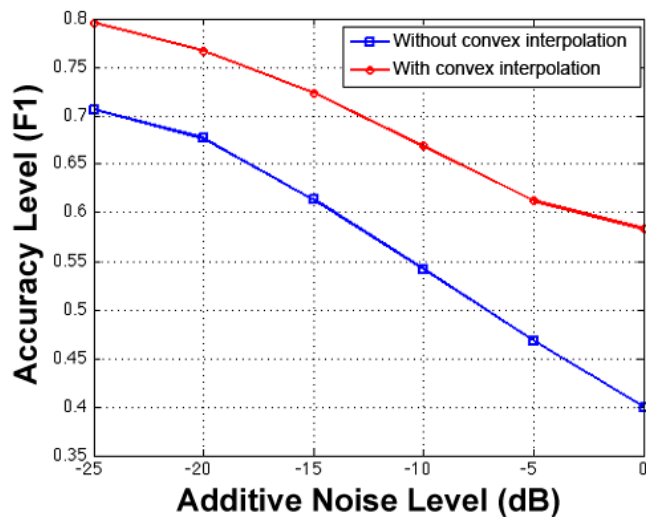

Fig. 10. The average performance of our algorithm with and without convex-hull interpolation vs. various levels of additive noise for 7 Patients (4, 5, 13, 14, 15, 19, and 29).
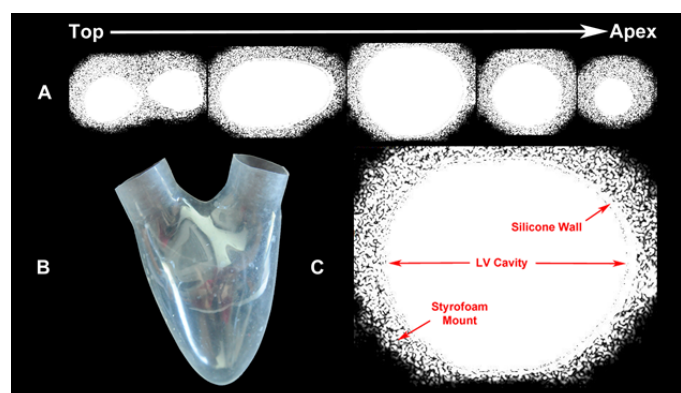

Fig. 11. (A) Top to apical view of select short axis MRI slices of the phantom. (B) The silicone model of the left ventricle used as a phantom in this experiment. (C) A mid ventricle slice with the components of the phantom labeled.

D. Phantom Validation and Reproducibility Study

To estimate the absolute accuracy of our segmentation method, a phantom was constructed with a known volume. The phantom is a simulation of a human LV including an inlet and an outlet (Figure 11). It is composed of transparent silicone rubber and shaped according to the shape of a human left ventricle in the diastolic state [32]. Our phantom was filled with 330 mL of

water mixed with 2mL of gadolinium, then held in a Styrofoam mold to keep it in place inside the MR scanner. Figure 11 is a composite image of the phantom and the corresponding MR images. Using a phantom provides flexibility with respect to validation since the chamber's volume is known, versus human data that needs to be calculated by other methods where each has its own inherent limitations.

After performing the 3D segmentation of the phantom, Simpson's rule was used to obtain the volume. The calculated volume was eventually compared to the known phantom volume of 332 mL. The algorithm was independently run for 10 times with different randomly-picked initiation point. The termination condition of the algorithm was set to 700 iterations or less than 0.0001% volume change in each iteration. Given these conditions, the 3D results took roughly two minutes to generate, and the algorithm returned values between 325 mL and 364 mL with a mean value of 345.2 ± 10.5 mL. These values correspond to an average error of $3.97\% \pm 3.16\%$ with a maximum error of 9.63% produced by the value of 364 mL, which was to some degree an outlier.
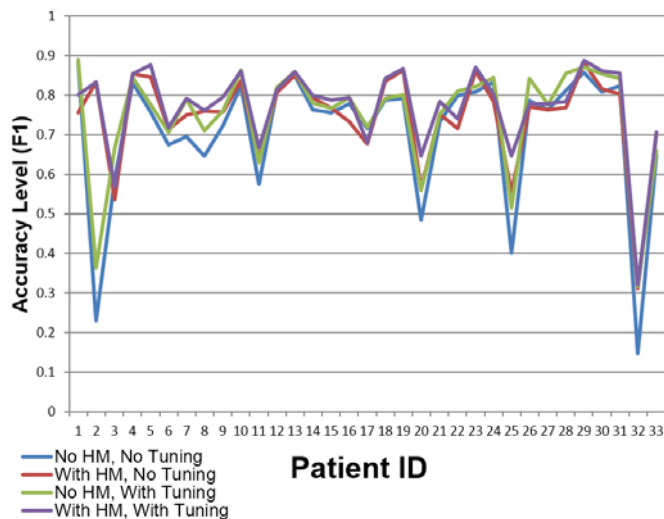

Fig. 12. Comparison between the algorithm's performance with and without using histogram matching (HM) and with and without fine-tuning. The plot is related to the York database that contains short axis cardiac MR images from 33 subjects together with their manual segmentations.

A similar performance was observed for the algorithm developed by Mille *et al.* [29] and Pluempitiwiriyawej *et al.* [17] (P>0.05). The reason for this similarity in performance is that the effect of the geometric term in our algorithm only comes to effect when the image quality is poor (e.g., human MR data) and as a result its effect on the performance of the phantom study was nil. The method described by Grosgeorge *et al.* [14], resulted in an average error of 10.6% compared to 3.97% for our algorithm.

E. Effect of Histogram Matching and Weight Fine-tuning

This section provides a performance comparison between the fine-tuned and fixed weights, as combined with and without histogram matching for all patients in the dataset. From Figure 12, it can be inferred that the histogram matching results

generally outperform the other results. More importantly, fine-tuning the weights would not improve the performance significantly if a set of fixed yet appropriate weights were used. In other words, the performance does not seem to be sensitive to the weights. We noticed that the histogram matching without fine-tuning occasionally achieves a better performance compared to that of the fine-tuned weights without histogram matching. Using Patient 13 as our main reference, we achieved the parameters mentioned in Table 2 for the best 3D active contour.

IV. DISCUSSION

The need for an efficient, accurate, and automated segmentation method has stimulated a large body of work in automated 3D CMR segmentation. Currently no singular approach has resulted in an accurate and fast segmentation algorithm that requires no prior statistical model or strong prior knowledge of the chamber's shape [2]. The current automated segmentation approaches are model-based (e.g. Active appearance model [AAM] [33] and active shape model [ASM] [5, 6]) and incorporate prior knowledge about the chamber that relies on a statistical model created from a large database of manually-segmented images.

Overall, the model-based approaches demonstrate adequate segmentation performance once the dataset is sufficiently large [34, 35]. Small datasets incur a large bias to the segmentation, making these methods ineffective when the heart shape is outside the learning set [34], which is likely to occur in the case of many cardiovascular diseases since the learning sets are primarily composed of normal images. Yet another challenge is to obtain large segmented datasets, which must be addressed using model-based approaches. An additional limitation of model-based algorithms is that the training data must be in the same format as the testing data; for example, if the training data are constructed using short-axis CMR images, they cannot be used for long-axis image segmentation [35].

There is a paucity of automated segmentation techniques and those that do exist have significant limitations, particularly the 3D reconstruction tools. Among these studies, early attempts at thresholding [36] were followed by the popular pixel classification [15, 16], active contour approaches [13, 14] and region based approaches [14, 29]. However, none of these approaches has resulted in an accurate and fast segmentation algorithm that requires no prior statistical model or strong prior knowledge of the shape of a chamber [2]. Additionally, to obtain a 3D segmented image, a common approach is to automate consecutive "2D segmentation" followed by "3D multiplanar reconstruction" steps. However, this approach fails to exploit the benefits of a true, 3D volumizing technique. Most segmentation approaches in 2D cannot readily handle cases where an object of interest (e.g., papillary muscles) appears to be separated into several cross-sections (i.e., non-convex object). This separation and discontinuity is commonly seen in CMR images, which incurs further challenges in 2D segmentation.

The novel method presented here performs simultaneous segmentation and three-dimensional reconstruction in a variety of patients as described in Table 1, and can also use any standard MR images (axial, coronal, or sagittal), along with both short- and long-axis CMR data.

As with any work, there are limitations to our study. One limitation is that our algorithm requires the input MR data to have a small slice thickness/interslice gap to generate a highly accurate 3D segmentation. There is no absolute number, but less than or equal to 8 mm would be ideal. With modern MR technology with increased resolution, this should not generally be an issue. Increased slice thickness results in an inaccurate mathematical derivative in the z-direction. Although not tested, the use of convex hull may not capture an LV with irregular borders such as the presence of LV aneurysm. Another limitation is that we are currently unable to provide a clear scheme that specifies exactly what quality level of an image is required to produce an ideal segmentation. We can only provide statistical results of our algorithm performance as we did in the numerical experiment section.

V. Conclusion

A true 3D reconstruction technique without the need for training datasets or any user-driven segmentation has been developed and validated. In this method, a novel combination of internal and external energy terms for active contour was utilized that exploits histogram matching for improving the segmentation performance. This method takes advantage of full volumetric imaging, does not rely on prior statistical knowledge and employs a convex hull interpolation to include the papillary muscles.

VI. Appendix

A. Region-based Term with Gaussian Distribution

For LV segmentation in the first step, the PDFs inside and outside of an active contour are modeled by Gaussian distributions with different means and variances. Applying this assumption to (4) results in

$$E_{reg} = \sum_{v \in \Omega} \left(\frac{|I(v) - c_1|^2}{\sigma_1^2} \left(1 - H(\Phi)\right) + \frac{|I(v) - c_2|^2}{\sigma_2^2} H(\Phi) \right)$$

(A.1)

where c_1, c_2, σ_1 and σ_2 are constant scalars that must be determined to minimize the region energy function (A.1). Following the argument in [19], one can show that c_1 and c_2 are optimized by

$$c_1 = \frac{\sum_{v \in \Omega} I(v)(1 - H(\Phi))}{\sum_{v \in \Omega}(1 - H(\Phi))} \text{ and } c_2 = \frac{\sum_{v \in \Omega} I(v)H(\Phi)}{\sum_{v \in \Omega} H(\Phi)} \quad \text{(A.2)},$$

and similarly,

$$\sigma_1^2 = \frac{\sum_{v \in \Omega}(I(v) - c_1)^2(1 - H(\Phi))}{\sum_{v \in \Omega}(1 - H(\Phi))}, \sigma_2^2 = \frac{\sum_{v \in \Omega}(I(v) - c_2)^2(H(\Phi))}{\sum_{v \in \Omega}(H(\Phi))} \text{ (A.3)}$$

Therefore, to minimize (A.1), we alternatively minimize over Φ assuming fixed c_1, c_2, σ_1 and σ_2, and then update the mean and variance parameters via (A.2) and (A.3).

B. Gradient Calculation of Internal and External Energy Functionals

Here, we invoke the Euler-Lagrange equality (9) for computing the gradient. In particular, the gradient of internal energy is calculated as

$$\frac{\partial E_{int}}{\partial \Phi} = -w_1 \left(\frac{\partial}{\partial x} \frac{\Phi_x}{\sqrt{\Phi_x^2 + \Phi_y^2 + \Phi_z^2}} \right.$$
$$+ \frac{\partial}{\partial y} \frac{\Phi_y}{\sqrt{\Phi_x^2 + \Phi_y^2 + \Phi_z^2}}$$
$$\left. + \frac{\partial}{\partial z} \frac{\Phi_z}{\sqrt{\Phi_x^2 + \Phi_y^2 + \Phi_z^2}} \right) \delta(\Phi(v))$$
$$= -w_1 Div \left(\frac{\nabla \Phi}{|\nabla \Phi|} \right) = -w_1 \kappa,$$

(B.1)

where κ is the contour curvature and $\delta(x)$ is the delta function. To obtain (B.1) from (9) and (2), we further used equality $|\nabla H(\Phi)| = |\nabla \Phi| \delta(\Phi)$ with $|\nabla \Phi| = 1$. Similarly, the gradient of different terms of external energy function with respect to Φ are obtained as

$$\frac{\partial E_{ext}}{\partial \Phi} = w_2 \frac{\partial E_{reg}}{\partial \Phi} + w_3 \frac{\partial E_{edge}}{\partial \Phi} + w_4 \frac{\partial E_{geom}}{\partial \Phi} \quad \text{(B.2)}$$

where

$$\frac{\partial E_{reg}}{\partial \Phi} = \left(\frac{(I(v) - c_1)^2}{\sigma_1^2} - \frac{(I(v) - c_2)^2}{\sigma_2^2} \right) \delta(\Phi), \quad \text{(B.3.)}$$

$$\frac{\partial E_{edge}}{\partial \Phi} = -\left(\nabla g(I(v)) \cdot \frac{\nabla \Phi}{|\nabla \Phi|} + g Div\left(\frac{\nabla \Phi}{|\nabla \Phi|}\right) \right) \delta(\Phi), \quad \text{(B.4.)}$$

and $$\frac{\partial E_{geom}}{\partial \Phi} = -\left(\frac{(x - \bar{x}) sign\left(E_{geom}^{(x)}\right) + (y - \bar{y}) sign\left(E_{geom}^{(y)}\right)}{\sum_\Omega (1 - H(\Phi(v)))} \right) \delta(\Phi)$$

(B.5)

in which $\bar{x}$ and $\bar{y}$ are the x-axis and y-axis mean of the contour's inside, i.e.,

$$\bar{x} = \frac{\sum_\Omega x (1 - H(\Phi(v)))}{\sum_\Omega 1 - H(\Phi(v))}, \bar{y} = \frac{\sum_\Omega y (1 - H(\Phi(v)))}{\sum_\Omega 1 - H(\Phi(v))} \quad \text{(B.6)}$$

and $E_{geom}^{(x)}$ and $E_{geom}^{(y)}$ are the terms specified in (6). To derive (B.5), we use the absolute value rule that states $\partial |f| = \partial f \, sign(f)$ where $sign(f)$ is the sign function. Although (B.5) seems to be independent of the initial input (x_0, y_0) at the first glance, it is not, and the effect of (x_0, y_0) appears in the $E_{geom}^{(x)}$ and $E_{geom}^{(y)}$ terms defined in (6). The 3D partial differential equations were discretized using *upwind scheme* [22] and the curvature in (B.1) was computed via *difference of normal method* outlined in [37].

REFERENCES

[1] M. Janik, M. D. Cham, M. I. Ross, Y. Wang, N. Codella, J. K. Min, M. R. Prince, S. Manoushagian, P. M. Okin, R. B. Devereux, and others, "Effects of papillary muscles and trabeculae on left ventricular quantification: increased impact of methodological variability in patients with left ventricular hypertrophy," *Journal of hypertension,* vol. 26, pp. 1677-1685, 2008.

[2] C. Petitjean and J.-N. Dacher, "A review of segmentation methods in short axis cardiac MR images," *Medical image analysis,* vol. 15, pp. 169-184, 2011.

[3] V. Tavakoli and A. A. Amini, "A survey of shaped-based registration and segmentation techniques for cardiac images," *Computer Vision and Image Understanding,* vol. 117, pp. 966-989, 2013.

[4] W. H. Luk, A. W. San Au-Yeung, A. X. N. Lo, T. K. L. Loke, and T. W. Ng, "Comparing Left Ventricular Ejection Fraction Measurement Using Cardiovascular Magnetic Resonance Imaging," *Radiologic technology,* vol. 85, pp. 494-499, 2014.

[5] H. C. Van Assen, M. G. Danilouchkine, A. F. Frangi, S. n. Ord s, J. J. Westenberg, J. H. Reiber, and B. P. Lelieveldt, "SPASM: a 3D-ASM for segmentation of sparse and arbitrarily oriented cardiac MRI data," *Medical image analysis,* vol. 10, pp. 286-303, 2006.

[6] M. R. Kaus, J. v. Berg, J. Weese, W. Niessen, and V. Pekar, "Automated segmentation of the left ventricle in cardiac MRI," *Medical image analysis,* vol. 8, pp. 245-254, 2004.

[7] M.-P. Jolly, "Automatic segmentation of the left ventricle in cardiac MR and CT images," *International Journal of Computer Vision,* vol. 70, pp. 151-163, 2006.

[8] T. Heimann and H.-P. Meinzer, "Statistical shape models for 3D medical image segmentation: A review," *Medical image analysis,* vol. 13, pp. 543-563, 2009.

[9] Y. Lu, P. Radau, K. Connelly, A. Dick, and G. Wright, "Segmentation of Left Ventricle in Cardiac Cine MRI: An Automatic Image-Driven Method," in "*Functional Imaging and Modeling of the Heart: 5th International Conference, FIMH*" *2009,* Nice, France, June 3-5, 2009, PP 339-347.

[10] Y. Zheng, A. Barbu, B. Georgescu, M. Scheuering, and D. Comaniciu, "Four-chamber heart modeling and automatic segmentation for 3-D cardiac CT volumes using marginal space learning and steerable features," *Medical Imaging, IEEE Transactions on,* vol. 27, pp. 1668-1681, 2008.

[11] C. Li, X. Jia, and Y. Sun, "Improved semi-automated segmentation of cardiac CT and MR images," in *Biomedical Imaging: From Nano to Macro, 2009. ISBI'09. IEEE International Symposium on*, 2009, pp. 25-28.

[12] A. Andreopoulos and J. K. Tsotsos, "Efficient and generalizable statistical models of shape and appearance for analysis of cardiac MRI," *Medical Image Analysis,* vol. 12, pp. 335-357.

[13] C. Xu, D. L. Pham, and J. L. Prince, "Image segmentation using deformable models," *Handbook of medical imaging,* vol. 2, pp. 129-174, 2000.

[14] D. Grosgeorge, C. Petitjean, J. Caudron, J. Fares, and J.-N. Dacher, "Automatic cardiac ventricle segmentation in MR images: a validation study," *International journal of computer assisted radiology and surgery,* vol. 6, pp. 573-581, 2011.

[15] A. Pednekar, U. Kurkure, R. Muthupillai, S. Flamm, and I. A. Kakadiaris, "Automated left ventricular segmentation in cardiac MRI," *Biomedical Engineering, IEEE Transactions on,* vol. 53, pp. 1425-1428, 2006.

[16] M. Lynch, O. Ghita, and P. F. Whelan, "Automatic segmentation of the left ventricle cavity and myocardium in MRI data," *Computers in Biology and Medicine,* vol. 36, pp. 389-407, 2006.

[17] C. Pluempitiwiriyawej, J. M. F. Moura, Y.-J. L. Wu, and C. Ho, "STACS: new active contour scheme for cardiac MR image segmentation," *Medical Imaging, IEEE Transactions on,* vol. 24, pp. 593 -603, may 2005.

[18] R. Malladi, J. A. Sethian, and B. C. Vemuri, "Shape modeling with front propagation: A level set approach," *Pattern Analysis and Machine Intelligence, IEEE Transactions on,* vol. 17, pp. 158-175, 1995.

[19] T. F. Chan and L. A. Vese, "Active contours without edges," *Image Processing, IEEE Transactions on,* vol. 10, pp. 266-277, 2001.

[20] M. Kass, A. Witkin, and D. Terzopoulos, "Snakes: Active contour models," *International Journal of Computer Vision,* vol. 1, pp. 321-331, 1988.

[21] T. Wang, B. Han, and J. Collomosse, "TouchCut: Fast image and video segmentation using single-touch interaction " *Computer Vision and Image Understanding,* vol. In process, 2013.

[22] M. Sussman, P. Smereka, and S. Osher, "A level set approach for computing solutions to incompressible two-phase flow," *Journal of Computational physics,* vol. 114, pp. 146-159, 1994.

[23] S. Osher and R. Fedkiw, *Level set methods and dynamic implicit surfaces* vol. 153: Springer Science & Business Media, 2003.

[24] R. C. Gonzalez and R. E. Woods, "Digital image processing, 2nd," *SL: Prentice Hall,* 2002.

[25] L. A. Vese and T. F. Chan, "A multiphase level set framework for image segmentation using the Mumford and Shah model," *International Journal of Computer Vision,* vol. 50, pp. 271-293, 2002.

[26] M. I. S. Franco P. Preparata, *Computational Geometry, Chapter "Convex Hulls: Basic Algorithms"*: Springer, 1985.

[27] A. P. Dempster, N. M. Laird, and D. B. Rubin, "Maximum likelihood from incomplete data via the EM algorithm," *Journal of the Royal Statistical Society. Series B (Methodological),* pp. 1-38, 1977.

[28] I. Ben Ayed, K. Punithakumar, S. Li, A. Islam, and J. Chong, "Left Ventricle Segmentation via Graph Cut Distribution Matching," in *Medical Image Computing and Computer-Assisted Intervention – MICCAI 2009.* vol. 5762, G.-Z. Yang, D. Hawkes, D. Rueckert, A. Noble, and C. Taylor, Eds., ed: Springer Berlin Heidelberg, 2009, pp. 901-909.

[29] J. Mille, R. Boné, P. Makris, and H. Cardot, "Segmentation and tracking of the left ventricle in 3D MRI sequences using an active surface model," in *Computer-Based Medical Systems, Twentieth IEEE International Symposium on*, ed, 2007, pp. 257-262.

[30] K. A. Kadir, A. Payne, J. J. Soraghan, and C. Berry, "Automatic left ventricle segmentation in T2 weighted CMR images," in *Image Processing and Communications Challenges 2*, ed: Springer, 2010, pp. 247-254.

[31] F. Sardanelli, M. Quarenghi, G. Di Leo, L. Boccaccini, and A. Schiavi, "Segmentation of cardiac cine MR images of left and right ventricles: interactive semiautomated methods and manual contouring by two readers with different education and experience," *Journal of Magnetic Resonance Imaging,* vol. 27, pp. 785-792, 2008.

[32] A. Falahapisheh and A. Kheradvar, "High-Speed Particle Image Velocimetry to Assess Cardiac Fluid Dynamics in vitro: From Performance to Validation," *European Journal of Mechanics - B/Fluids,* vol. 35, pp. 2-8, 2012.

[33] S. C. Mitchell, J. G. Bosch, B. P. F. Lelieveldt, R. J. van der Geest, J. H. C. Reiber, and M. Sonka, "3-D active appearance models: segmentation of cardiac MR and ultrasound images," *Medical Imaging, IEEE Transactions on,* vol. 21, pp. 1167-1178, 2002.

[34] X. Bresson, P. Vandergheynst, and J.-P. Thiran, "A variational model for object segmentation using boundary information and shape prior driven by the Mumford-Shah functional," *International Journal of Computer Vision,* vol. 68, pp. 145-162, 2006.

[35] M. R. Avendi, A. Kheradvar, and H. Jafarkhani, "A combined deep-learning and deformable-model approach to fully automatic segmentation of the left ventricle in cardiac MRI," *Medical Image Analysis,* vol. 30, pp. 108-119, 2016.

[36] A. Goshtasby and D. A. Turner, "Segmentation of cardiac cine MR images for extraction of right and left ventricular chambers," *Medical Imaging, IEEE Transactions on,* vol. 14, pp. 56-64, 1995.

[37] A. E. Lefohn, J. M. Kniss, C. D. Hansen, and R. T. Whitaker, "A streaming narrow-band algorithm: interactive computation and visualization of level sets," in *ACM SIGGRAPH 2005 Courses*, 2005, p. 243.